Published in the International Journal of Solids and Structures, vol. 36 No. 31/32 pages 4901-4918, 1999.

A Model for Elastic–Plastic Pressure Sensitive Materials Subjected to Large Deformations

Boris Jeremić [1] **Kenneth Runesson** [2] **Stein Sture** [3]

[1] Assistant Professor,
Department of Civil and Environmental Engineering,
Clarkson University, Potsdam, NY, 13699, U.S.A.
phone (315) 268-4435, fax (315) 268-7985
Email: Jeremic@Polaris.Clarkson.edu

[2] Professor,
Division of Solid Mechanics,
Chalmers University of Technology, S-41296 Göteborg, Sweden
Email: KeRu@Solid.Chalmers.SE

[3] Professor and Chairman,
Department of Civil, Environmental, and Architectural Engineering,
University of Colorado, Boulder, CO 80309-0428, U.S.A.
Email: Stein.Sture@Civil.Colorado.edu

Abstract

Development of a finite deformation elasto-plastic model for pressure sensitive materials is presented. The chosen model, which has its roots in the MRS–Lade material model (cf. [18]) is influenced by recent developments by [7]. The thermodynamic consequences of introducing non-associative yielding (both deviatoric and volumetric) and hardening/softening characteristics are assessed. The consistently linearized Algorithmic Tangent Stiffness (ATS) tensor is presented. This tensor is used in the constitutive driver as a key feature of the efficient iterative procedure for satisfying equilibrium in the case of stress (or mixed) control.

The chosen model is calibrated using data from experiments conducted in a Directional Shear Cell (DSC), which has been used extensively at the University of Colorado at Boulder to investigate the behavior of pressure sensitive materials under deformations of large magnitude.

Key Words: Hyperelasto–plasticity, Large Deformations, Geomaterials, Finite element analysis

1 Introduction

A wealth of literature has been devoted to the development of plasticity models intended to represent the response of granular materials under quasistatic loading. The typical characteristics to be incorporated in a realistic model are, among others (a) an initial yield surface that depends on all three stress invariants[1], (b) dilatancy characteristics that are of the "non-associative" type, (c) elasto–plastic coupling in the sense that the elastic moduli depend on the inelastic volume change, (d) hardening–softening behavior that depend on the effective pressure, and (e) the possibility for non-homogeneous deformation (shear banding) that is promoted by dilatancy and softening. Among the relevant literature, we mention [8], [13], [14], [3], [16].

[1] In the most ideal situation when the material is preconsolidated isotropically.

A versatile model must be useful for a wide range of effective pressures, including the very low confinement region in which case the shear stresses are also small. The later situation is of great importance in liquefaction problems and μ–gravity environments. The low gravity problem has attracted some attention in recent years, from both experimental viewpoint, cf. [1], as well as with regard to modeling, cf. [18]. The small stress region poses particularly challenging problems. For example, the sharp curvature in the meridian plane for the yield surface requires a carefully designed strategy for integrating the constitutive relations.

Most plasticity models for pressure–sensitive materials have been proposed in a small deformation setting, although there is ample evidence of large strain situations in engineering practice. In order to discern the properties under large amounts of shear, without introducing large rotations (like in the simple shear test), the Directional Shear Cell (DSC) was developed by [19]. By using these experimental data, uncertainties in the model related to large rotations can be avoided. On the other hand, one might argue that a model that has been calibrated for DSC–results may give poor results in the simple shear test due to possible inherent adequacies in dealing with rotations. Hence, these types of test data should be complementary in a comprehensive calibration effort.

In this paper we propose a new model, which is an improved version of the MRS–Lade model (cf. [18]), in several respects. As to the large strain environment both the hypoelastic end hyperelastic formats are employed to provide a comparison. Whereas the hypoelastic format is classical in conjunction with pressure–sensitive materials, cf. [11], [12], it appears that very few attempts have been made to use the hyperelastic format. One of those is by [2]. It is expected from other investigations on metal behavior that the difference in performance is small for the present case of isotropic hardening, and this assumption is indeed confirmed by the computational results in the paper.

The paper is organized as follows: In Section 2 we review the basic assumptions underlying the hypoelastic format (employing McInnis rate) as well as the hyperelastic format of elasto-plasticity. The proposed B–model is described in some detail in Section 3, whereas integration

issues (general and specific to the B–model) are discussed in Section 4. The paper is concluded by some computational results in Section 5 relating to the DSC apparatus.

2 Large Strain Elasto-plasticity with Isotropic Hardening

2.1 Preliminaries

The classical approach to deal with large strains is to employ the hypoelastic–plastic format, whereby the relations from the small strain theory are adopted with the difference that the ordinary time rates of stress and strain are replaced by suitable objective rates. Particularly in conjunction with kinematic hardening, it is well–known that the choice of stress rate is crucial in order to avoid pathological behavior for large rotations (cf. [10]). However, the hypoelastic format is conceptually questionable since it lacks a firm thermodynamic basis.

In recent years there has been a strong emphasis on the hyperelastic–plastic format, which employs the concept of a stress–free intermediate configuration (denoted $\bar{\Omega}$ subsequently). The constitutive relations are derivable within a thermodynamic framework, which provides a possibility to discern the thermodynamic admissibility of any particular explicit choice of model.

A summary of pertinent relations for both formats will be given subsequently.

2.2 Hypoelastic–Plastic Format

Adopting the additive split of the spatial strain rate tensor d_{ij}, we consider the generic tangent relation

$$\overset{*}{\tau}_{ij} = \mathcal{E}^e_{ijkl}\ (d_{kl} - d^p_{kl}) \tag{1}$$

where $\overset{*}{\tau}_{ij}$ denotes an objective rate of Kirchhoff stress τ_{ij} $(= J\ \sigma_{ij})$. Here we choose, for definiteness, the McInnis rate defined as

$$\overset{*}{\tau}_{ij} = \dot{\tau}_{ij} + \tau_{ik}\Omega_{kj} - \Omega_{ik}\tau_{kj} \qquad , \qquad \Omega_{ij} = \dot{R}_{ik}(R_{kj})^t \tag{2}$$

where R_{ij} is the actual material rotation. Moreover, $\mathcal{E}^e_{ijkl}$ is the *constant* elastic stiffness tensor derived for small deformations. It is defined in terms of the shear modulus G and the bulk modulus K_b in the case of elastic isotropy (which will be assumed here).

In the case of isotropic hardening, governed by the scalar "hardening stress" K_α , $\alpha = 1, 2, \cdots$, we may define plastically admissible states as those contained in the convex set $\mathcal{B}$

$$\mathcal{B} = \{\tau_{ij}, K_\alpha \mid \Phi(\tau_{ij}, K_\alpha) \leq 0\} \tag{3}$$

where Φ is the yield function. Upon introducing the plastic potential $\Phi^*(\tau_{ij}, K_\alpha)$, we may define non-associative flow and hardening rules to obtain the following set of constitutive rate equations

$$\overset{*}{\tau}_{ij} = \mathcal{E}^e_{ijkl}\ d_{kl} - \dot{\mu}\ \mathcal{E}^e_{ijkl}\ f^*_{kl} \qquad \text{with} \qquad f^*_{kl} = \frac{\partial \Phi^*}{\partial \tau_{kl}} \tag{4}$$

$$K_\alpha = K_\alpha(\kappa_\beta) \quad , \quad \dot{\kappa}_\beta = \dot{\mu}\ \frac{\partial \Phi^*}{\partial K_\beta} \quad , \quad \kappa_\beta(0) = 0 \tag{5}$$

where we have introduced internal variables[2] κ_β. Moreover, no elastic–plastic coupling is included. The plastic multiplier $\dot{\mu}$ is determined from the loading conditions[3]

$$\dot{\mu} \geq 0 \qquad , \qquad \Phi \leq 0 \qquad , \qquad \dot{\mu}\ \Phi = 0 \tag{6}$$

It is convenient to express the constitutive relations in the "rotation–neutralized" format, which is obtained upon a pull–back of the relation (4) to a rotated configuration Ω^{RN}. This is achieved upon introducing the variables

$$\tau^{RN}_{ij} = (R_{ik})^t\ \tau_{kl}\ R_{lj} \quad , \quad d^{RN}_{ij} = (R_{ik})^t\ d_{kl}\ R_{lj} \tag{7}$$

[2]The terminology from thermodynamics is used for convenience, while realizing that it is strictly relevant only for small strains (since the hypoelastic format is adopted).

[3]These are the Kuhn–Tucker complementary conditions in the special case of fully associative theory, defining the Standard Dissipative Material, cf. [4].

whereby (4) is replaced by

$$\dot{\tau}_{ij}^{RN} = \mathcal{E}_{ijkl}^{e}\, d_{kl}^{RN} - \dot{\mu}\, \mathcal{E}_{ijkl}^{e}\, f_{kl}^{*,RN} \quad , \quad f_{kl}^{*,RN} = (R_{ki})^{t}\, d_{ij}\, R_{jl} \tag{8}$$

It is noted that $\mathcal{E}_{ijkl}^{e}$ do not change during the rotation transformation due to the assumed isotropy. Moreover, since the hardening variables are scalar quantities, they remain unchanged during rotation and, hence, (5) does not change. After integration of τ_{ij}^{RN} and K_α, then a push–forward to the spatial format using (7) gives τ_{ij}.

2.3 Hyperelastic–Plastic Format

We propose the free energy density ψ, which is defined in $\bar{\Omega}$, as follows

$$\rho_0 \psi(\bar{C}_{ij}^{e}, \kappa_\alpha) = \rho_0 \psi^{e}(\bar{C}_{ij}^{e}) + \rho_0 \psi^{p}(\kappa_\alpha) \tag{9}$$

where $\psi^{e}(\bar{C}_{ij}^{e})$ represents a suitable hyperelastic model in terms of the elastic right deformation tensor $\bar{C}_{ij}^{e}$, whereas $\psi^{p}(\kappa_\alpha)$ represents the hardening. It has been shown elsewhere, e.g. [5], that the pertinent dissipation inequality becomes

$$D = \bar{T}_{ij}\, \bar{L}_{ij}^{p} + \sum_{\alpha} K_\alpha\, \dot{\kappa}_\alpha \geq 0 \tag{10}$$

where $\bar{T}_{ij}$ is the Mandel stress and $\bar{L}_{ij}^{p}$ is the plastic velocity gradient defined on intermediate configuration $\bar{\Omega}$.

Remark 2.1 A different form of (10) may be employed in the case of non-isotropic, e.g. kinematic hardening.

We now define $\mathcal{B}$ as

$$\mathcal{B} = \{\bar{T}_{ij}, K_\alpha \mid \Phi(\bar{T}_{ij}, K_\alpha) \leq 0\} \tag{11}$$

When Φ is isotropic in $\bar{T}_{ij}$ (which is the case here) in conjunction with elastic isotropy, we can conclude that $\bar{T}_{ij}$ is symmetrical and we may replace $\bar{T}_{ij}$ by τ_{ij} in Φ.

As to the choice of elastic law, it is emphasized that this is largely a matter of convenience since we shall be dealing with small elastic deformations. Here, the Neo–Hookean elastic law is adopted. The generic situation is $\bar{T}_{ij} = \bar{T}_{ij}(\tilde{\bar{U}}^e_{kl}, \bar{J}^e)$, where we have used the isochoric/volumetric split of the elastic right stretch tensor as $\bar{U}^e_{kl} = \tilde{\bar{U}}^e_{kl}\,(\bar{J}^e)^{1/3}$.

The constitutive relations can now be written as

$$\bar{T}_{ij} = \bar{T}_{ij}(\tilde{\bar{U}}^e_{kl}, \bar{J}^e) \quad , \quad \bar{L}^p_{ij} := \dot{F}^p_{ik}\,\left(F^p_{jk}\right)^{-1} = \dot{\mu}\frac{\partial \Phi^*}{\partial \bar{T}_{ij}} = \dot{\mu}\bar{M}_{ij} \tag{12}$$

$$K_\alpha = K_\alpha(\kappa_\beta) \quad , \quad \dot{\kappa}_\beta = \dot{\mu}\,\frac{\partial \Phi^*}{\partial K_\beta} \quad , \quad \kappa_\beta(0) = 0 \tag{13}$$

where $F^p_{ik} = (\bar{F}^e_{li})^{-1}F_{lk}$ is the plastic part of the deformation gradient. The plastic multiplier $\dot{\mu}$ is defined by the loading conditions formally given in (6).

3 B–Model for Cohesionless Granular Material

3.1 Preliminaries

In this section we give a review of the various concepts and characteristic features of the adopted constitutive model (subsequently denoted the B–Model). This model relies on the development behind the so called MRS–Lade model [18]. There are many differences between the MRS–Lade model and the B–Model (for small strains). In particular the deviatoric trace of the yield surface is in the B–Model is based on the work of [7]. The shape of the deviatoric trace depends on the effective pressure in a realistic fashion, which was not included in the MRS–Lade model. The B–Model is a single surface model, with uncoupled cone portion and cap portion hardening. Special attention was given to the very low confinement region, where the yield surface was shaped in a such way to mimic recent[4] higher friction angle findings for the that stress region.

[4]Micro Gravity Mechanics tests aboard Space Shuttle.

Box 3.1 Analytic relations for the B–Model.

1. Yield Function

$$\Phi\left(p,q,\theta;\eta,p_c\right) = q^2 - \Phi_{dev}\left(p,\theta;p_c\right)\Phi_{mer}\left(p,\eta;p_c\right)$$

$$\Phi_{dev}\left(p,\theta;p_c\right) = \left(\sqrt{\frac{2}{3}}\cos\left(\frac{1}{3}\arccos\left(\gamma\left(p\right)\cos\left(3\theta\right)\right)\right)\right)^{-2}$$

$$\gamma\left(p;p_c\right) = \frac{1}{2} + \frac{1}{\pi}\arctan\left(\frac{-a\ \left(p - b\ \left(p_c - p_t\right)\right)}{p_c - p_t}\right) \qquad \gamma \in (0,1)$$

$$\Phi_{mer}\left(p;\eta,p_c\right) = \Phi_{ell}\left(p;p_c\right)\ \Phi_{alt}\left(p;\eta\right)$$

$$\Phi_{ell}\left(p;p_c\right) = R - \frac{\left(p - p_t\right)^2}{\left(p_c - p_t\right)^2}$$

$$\Phi_{alt}\left(p;\eta\right) = \left(\frac{\left(p - p_t\right)\ \left(b_1\,\eta_{init} + \eta\ \left(\eta_{init}\,p + \eta\ \left(-p + p_t\right)\right)\right)}{b_1 - \eta\,p + \eta_{init}\,p + 2\,\eta\,p_t - \eta_{init}\,p_t}\right)^2$$

2. Hardening Functions

$$\eta\left(\kappa_{cone}\right) = \frac{d\,\eta_{res}\,{\kappa_{cone}}^2 + \frac{d\left(\eta_{peak} - \eta_{res}\right)\eta_{start}\,{\kappa_{peak}}^2}{\eta_{peak} - \eta_{start}} + \kappa_{cone}\ \left(e\,\eta_{peak} + 2\,d\ \left(\eta_{peak} - \eta_{res}\right)\ \kappa_{peak}\right)}{e\,\kappa_{cone} + d\,{\kappa_{cone}}^2 + \frac{d\left(\eta_{peak} - \eta_{res}\right)\kappa_{peak}{}^2}{\eta_{peak} - \eta_{start}}}$$

$$p_c\left(\kappa_{cap}\right) = p_{c,0}\left(1 + \left(\kappa_{cap}\right)^{\frac{1}{r}}\right)$$

3. Plastic potential – flow rule

$$\Phi^*\left(p,q,\theta;\eta,p_c\right) = q^2 - \Phi_{dev}\left(p,\theta\right)\Phi^*_{mer}\left(p;\eta,p_c\right)$$

$$\Phi^*_{mer}\left(p;\eta,p_c\right) = n\ \Phi_{mer}\left(p;\eta,p_c\right)$$

4. Hardening–softening rules

$$\dot{\kappa}_{cone} = \frac{S_{cone}(p)}{c_{cone}p_a}\left(\frac{p - p_t}{p_{ref}}\right)^{-l}\ \bar{T}_{ij}\ \bar{L}^p_{ij} \qquad S_{cone}\left(p\right) = \frac{1}{2} + \frac{1}{\pi}\arctan\left(\frac{-a_s\ \left(p - b_s\ \left(p_c - p_t\right)\right)}{p_c - p_t}\right)$$

$$\dot{\kappa}_{cap} = \frac{S_{cap}(p)}{c_{cap}p_a}\left(\frac{p_{a,0}}{p_{ref}}\right)^{-r}\ \bar{T}_{ij}\ \bar{L}^p_{ij} \qquad S_{cap}\left(p\right) = \frac{1}{2} + \frac{1}{\pi}\arctan\left(\frac{a_s\ \left(p - b_s\ \left(p_c - p_t\right)\right)}{p_c - p_t}\right)$$

The present generalization to the large strain setting is quite trivial from the point of view of describing yield and potential surfaces: The true stress σ_{ij} is replaced by the Mandel stress $\bar{T}_{ij}$. However, since the yield function is isotropic, hardening is of isotropic type and isotropic elasticity is assumed, it turns out that the invariants of T_{ij} become equal to the invariants of the Kirchhoff stress τ_{ij}. Hence, in the various functions involved in describing the constitutive relations, we shall employ the invariants of τ_{ij} defined as

$$p = -\frac{1}{3}\tau_{kk} \;\; ; \;\; q = \sqrt{\frac{3}{2}s_{ij}s_{ij}} \;\; ; \;\; \cos 3\theta = \sqrt{\frac{3}{2}}\frac{s_{ij}s_{jk}s_{ki}}{(s_{ij}s_{ij})^{\frac{3}{2}}} \;\; ; \;\; s_{ij} = \tau_{ij} - \frac{1}{3}\tau_{kk}\delta_{ij} \tag{14}$$

Stresses are chosen as positive in tension. The definition of Lode's angle θ in equation (14) implies that $\theta = 0$ defines the meridian of conventional triaxial extension (CTE), while $\theta = \pi/3$ denotes the meridian of conventional triaxial compression (CTC).

The various relations of the B–Model are listed in Box 3.1 for brevity and transparency. In the following subsections, we discuss these relations in some further details.

3.2 Yield and Failure Surfaces

The analytical form of the yield surface, which is identical to the failure surface in its extreme position corresponding to the peak value η_{peak} of the mobilized friction coefficient η, is given in Box 3.1. It is a "bullet–shaped", three invariant surface with its apex located at the origin of stress space for a cohesionless granular material. Apart from the apex, the surface is completely smooth[5], even at the transition between the "cone" and "cap" parts associated with dilatant and contractant behavior, respectively. The functions Φ_{dev} and Φ_{mer} control the shape in the deviatoric and meridian planes, respectively.

The meridian trace of the yield surface, which looks typically as shown in Figure 1, is defined by the two functions Φ_{ell} and Φ_{alt}. The function Φ_{ell} defines an elliptic trace, whereas the primary role of Φ_{alt} is to provide the appropriate behavior for low confinement pressures.

[5]In the sense that the gradient is continuous everywhere.

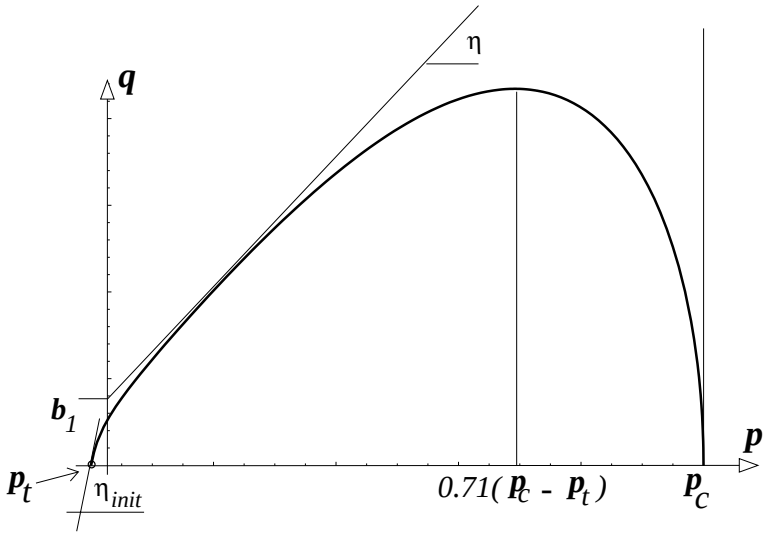

Figure 1: Meridian trace of yield, ultimate or potential surface.

In Particular, Figure 1 shows that the initial value[6] of the internal friction angle is defined by the value η_{init}.

As to the deviatoric contours of the yield surface, defined by the function Φ_{dev} in Box 3.1, they are based on the developments by [7]. The "shape function" $\gamma(p, p_c)$ defines the "triangularity" of the deviatoric trace along the hydrostatic axis. For low confinement pressures the shape is almost triangular, whereas it becomes close to circular for very large values of p, as shown in Figure 2. In order to accomplish this physically realistic result, $\gamma(p, p_c)$ is designed such that $\gamma(p \to p_t; p_c) \to 1$ whereas $\gamma(p \to p_c; p_c) \to 0$.

3.3 Flow and Hardening Rules

The flow rule is of the non-associative type and is defined by the plastic potential Φ^* as given in Box 3.1. It follows that the non-associativity is restricted to the volumetric response, which is controlled by the scalar n. Clearly, associative flow is retrieved when $n = 1$.

The hardening functions η (the mobilized friction) and p_c (the isotropic consolidation

[6] At the apex.

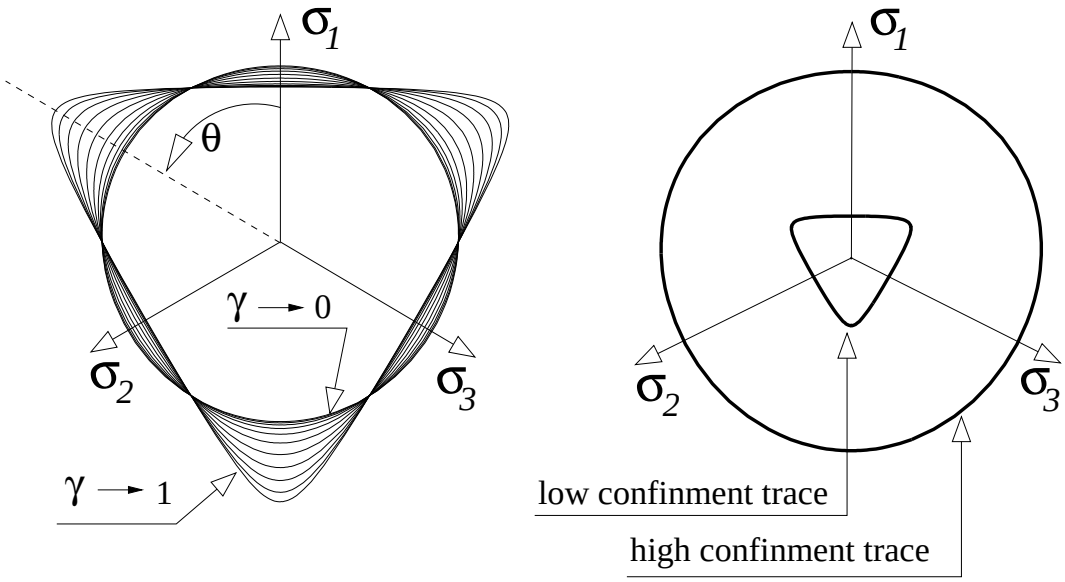

Figure 2: Evolution of deviatoric trace of yield surface with the Lode's angle θ, for different values of shape parameter γ, which changes along the mean stress axes.

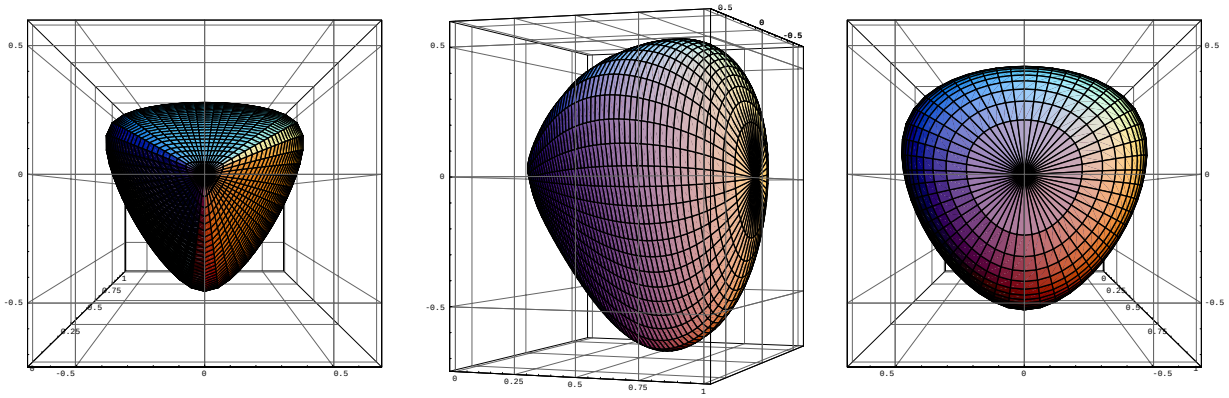

Figure 3: Yield surface in principal stress space (shown in extended form since for ordered principal stresses $\sigma_1 \geq \sigma_2 1 \geq \sigma_3$ only first sextant is valid).

pressure) are functions of the internal variables κ_{cone} and κ_{cap}, respectively, as given in Box 3.1 and in Figure 5. In the thermodynamic setting, η and p_c would be denoted the dissipative stresses. In order to complete the model, we need to define the hardening rules in terms of

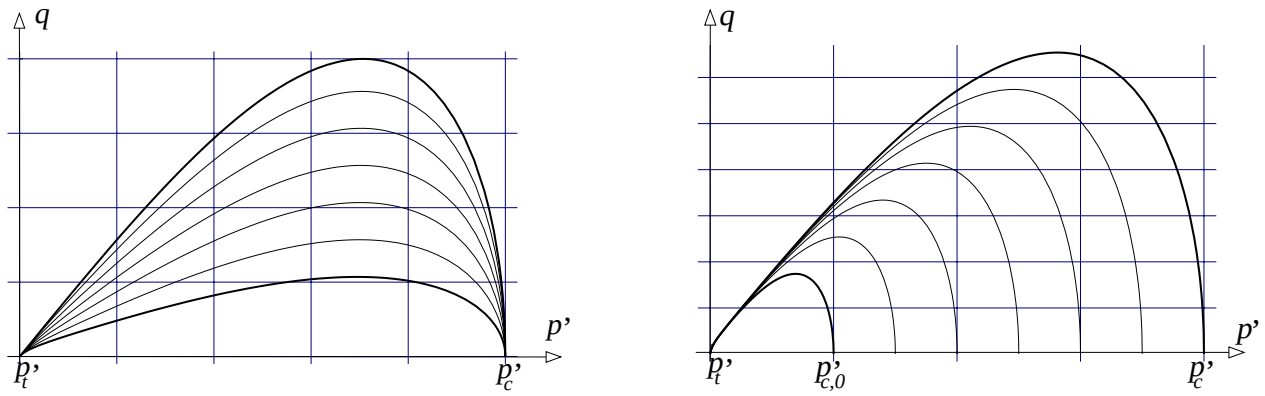

Figure 4: Evolution of yield surface with the mobilized friction parameter η and cap parameter p_c. Shown in meridian plane.

rate equations that define the evolution of η and p_c, which are given in Box 3.1.

The notion of "cone" and "cap" may seem unwarranted, since this model employs a single yield surface. However, it is convenient to distinguish the cone and cap regions by the maximum value of q in the meridian plane, c.f. Figure 1. The corresponding value of isotropic pressure defining the boundary between the two regions is simply obtained as $p = \sqrt{2}/2\ (p_c - p_t)$.

In order to control the hardening of the cone and cap portions separately, the "switch" functions $S_{cone}(p)$ and $S_{cap}(p)$ were introduced in the hardening rules. These are chosen as the requlatized Heaviside functions, cf. Box 3.1, whose steepness is controlled by the constant a_s, while the position of the switch is controlled by the constant b_s. The typical behavior of $S_{cone}(p)$ and $S_{cap}(p)$ is shown in Figure 6.

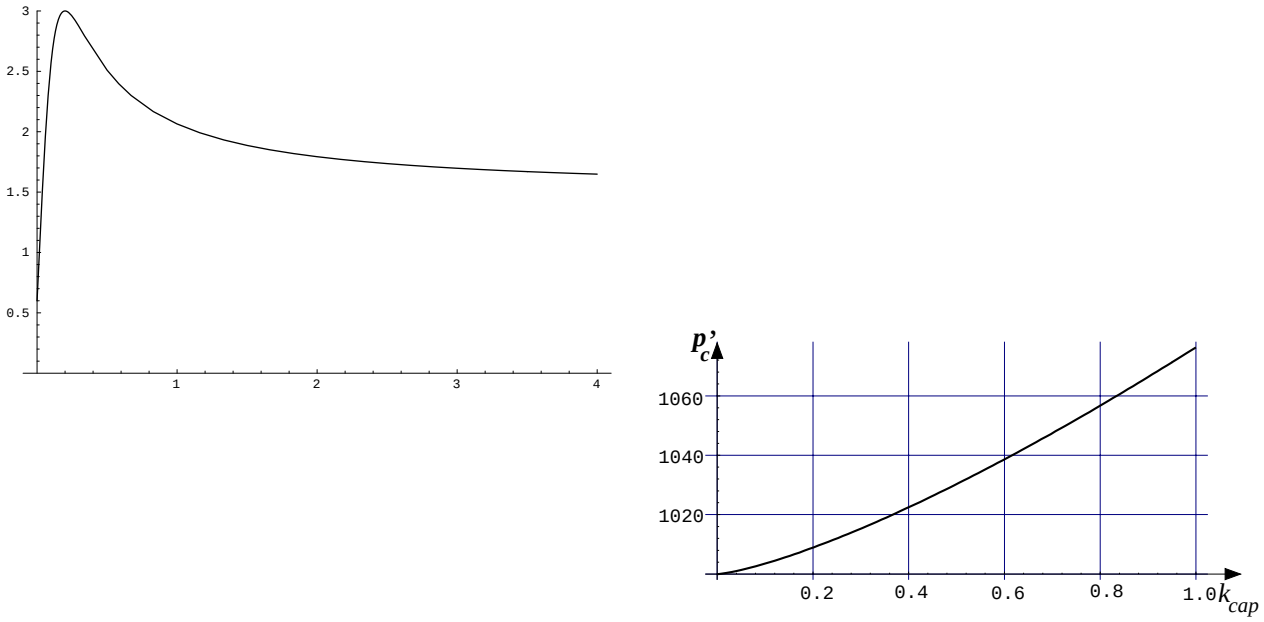

Figure 5: Cone and cap hardening functions.

4 Aspects on Integration of Constitutive Relations

4.1 Incremental Evolution Equations

The flow rule from equation (12) can be integrated to give

$$ {}^{n+1}F^{p}_{ij} = \exp\left(\Delta\mu\, {}^{n+1}\bar{M}_{ik}\right) {}^{n}F^{p}_{kj} \tag{15} $$

and by using multiplicative decomposition of deformation gradient we obtain

$$ {}^{n+1}\bar{F}^{e}_{ij} = {}^{n+1}\bar{F}^{e,tr}_{ik} \exp\left(-\Delta\mu\, {}^{n+1}\bar{M}_{kj}\right) \;\text{ with }\; {}^{n+1}\bar{F}^{e,tr}_{ik} = {}^{n+1}F_{im}\; \left({}^{n}F^{p}_{mk}\right)^{-1} \tag{16} $$

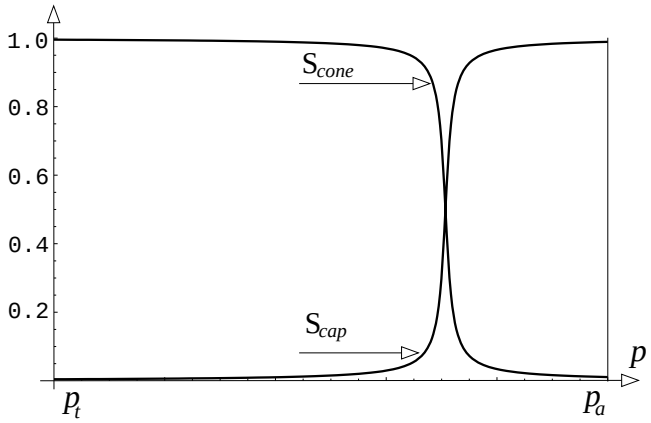

Figure 6: Plot of *switch* functions $S_{cone}(p)$, $S_{cap}(p)$ for $a_s = 100.0$ and $b_s = 0.707$.

The elastic deformation is then

$$ {}^{n+1}\bar{C}^{e}_{ij} \overset{\text{def}}{=} \left({}^{n+1}\bar{F}^{e}_{im}\right)^{T} {}^{n+1}\bar{F}^{e}_{mj} = \exp\left(-\Delta\mu^{n+1}\bar{M}^{T}_{ir}\right) {}^{n+1}\bar{C}^{e,tr}_{rl} \exp\left(-\Delta\mu^{n+1}\bar{M}_{lj}\right) \tag{17} $$

By recognizing that the exponent of a tensor can be expanded in Taylor's (MacLaurin's) series[7]

$$ \exp\left(-\Delta\mu^{n+1}\bar{M}_{lj}\right) = \delta_{lj} - \Delta\mu^{n+1}\bar{M}_{lj} + \frac{1}{2}\left(\Delta\mu^{n+1}\bar{M}_{ls}\right)\left(\Delta\mu^{n+1}\bar{M}_{sj}\right) + \cdots \tag{18} $$

we obtain

$$ {}^{n+1}\bar{C}^{e}_{ij} = {}^{n+1}\bar{C}^{e,tr}_{ij} - \Delta\mu^{n+1}\bar{M}_{ir}\ {}^{n+1}\bar{C}^{e,tr}_{rj} - \Delta\mu\ {}^{n+1}\bar{C}^{e,tr}_{il}\ {}^{n+1}\bar{M}_{lj} \tag{19} $$

The proposed algorithm uses MacLaurin's series expansion of integrated deformation tensors rather than the spectral decomposition, which is widely described in the literature, cf. [17]. Restriction posed by the use of spectral decomposition to isotropic yield criteria[8] is being removed.

[7] See for example [15].

[8] And especially the enforcement of collinearity between eigen–directions of elastic and plastic deformation tensors.

Remark 4.1 In the limit, when displacements are sufficiently small, the solution (19) collapses to a small deformation elastic predictor plastic corrector equation in strain space

$$^{n+1}\epsilon_{ij} \;=\; ^{n+1}\epsilon^{tr}_{ij} - \Delta\mu \; ^{n+1}\bar{M}_{ij} \tag{20}$$

The hardening rule (12) can be integrated to give

$$^{n+1}\kappa_\alpha = {}^{n}\kappa_\alpha + \Delta\mu \; \left.\frac{\partial \Phi^*}{\partial K_\alpha}\right|_{n+1} \tag{21}$$

The incremental problem is defined by equations (19), (21), the constitutive relations

$$^{n+1}\bar{S}_{IJ} = 2 \left.\frac{\partial W}{\partial C_{IJ}}\right|_{n+1} \tag{22}$$

$$^{n+1}K_\alpha = - \left.\frac{\partial W}{\partial \kappa_\alpha}\right|_{n+1} \tag{23}$$

the Kuhn–Tucker (KT) conditions

$$\Delta\mu < 0 \quad ; \quad ^{n+1}\Phi \leq 0 \quad ; \quad \Delta\mu \; ^{n+1}\Phi = 0 \tag{24}$$

This set of nonlinear equations will be solved with a Newton type procedure, described in next section.

4.2 The Integration Algorithm

The elastic predictor, plastic corrector equation

$$^{n+1}\bar{C}^{e}_{ij} = {}^{n+1}\bar{C}^{e,tr}_{ij} - \Delta\mu \; \left(^{n+1}\bar{M}_{ir} \; ^{n+1}\bar{C}^{e,tr}_{rj} \; + {}^{n+1}\bar{C}^{e,tr}_{il} \; ^{n+1}\bar{M}_{lj} \right) = {}^{n+1}\bar{C}^{e,tr}_{ij} - \Delta\mu \; ^{n+1}Z_{ij} \tag{25}$$

is used as a starting point for a Newton iterative algorithm. In the previous equation, we have introduced tensor Z_{ij} to shorten writing. The trial right elastic deformation tensor is defined as

$$^{n+1}\bar{C}^{e,tr}_{ij} = \left(^{n+1}\bar{F}^{e,tr}_{ri} \right)^T \; \left(^{n+1}\bar{F}^{e,tr}_{rj} \right) = \left(^{n+1}F_{rM} \; \left(^{n}F^{p}_{iM} \right)^{-1} \right)^T \; \left(^{n+1}F_{rS} \; \left(^{n}F^{p}_{jS} \right)^{-1} \right) \tag{26}$$

We define a tensor of deformation residuals

$$R_{ij} = \underbrace{\bar{C}^e_{ij}}_{current} - \underbrace{\left({}^{n+1}\bar{C}^{e,tr}_{ij} - \Delta\mu\ {}^{n+1}Z_{ij}\right)}_{BackwardEuler} \tag{27}$$

Tensor R_{ij} represents the difference between the current right elastic deformation tensor and the Backward Euler right elastic deformation tensor. The trial right elastic deformation tensor ${}^{n+1}\bar{C}^{e,tr}_{ij}$ is maintained fixed during the iteration process. By applying first order Taylor series expansion to (27) and solving for $d\bar{C}^e_{pq}$ one gets

$$d\bar{C}^e_{pq} = (\mathcal{T}_{mnpq})^{-1}\left(-R^{old}_{mn} - d(\Delta\mu)\ {}^{n+1}Z_{mn} + \Delta\mu\frac{\partial^{n+1}Z_{mn}}{\partial K_\alpha}\ d(\Delta\mu)\ H_{\alpha\beta}\ \frac{\partial\Phi^*}{\partial K_\beta}\right) \tag{28}$$

where it was used that

$$dK_\alpha = \frac{\partial K_\alpha}{\partial\kappa_\beta}\ d\kappa_\beta = -d(\Delta\mu)\ \frac{\partial K_\alpha}{\partial\kappa_\beta}\ \frac{\partial\Phi^*}{\partial K_\beta} = -d(\Delta\mu)\ H_{\alpha\beta}\ \frac{\partial\Phi^*}{\partial K_\beta} \tag{29}$$

$$\mathcal{T}_{mnpq} = \delta_{pm}\delta_{nq} + \Delta\mu\frac{\partial^{n+1}Z_{mn}}{\partial\bar{T}_{pk}}\ \left(\bar{C}^e_{sq}\right)^{-1}\ \bar{T}_{sk} + \frac{1}{2}\ \Delta\mu\frac{\partial^{n+1}Z_{mn}}{\partial\bar{T}_{ij}}\ \bar{C}^e_{ik}\ \bar{\mathcal{L}}^e_{kjpq} \tag{30}$$

By using a first order Taylor series expansion of a yield function and solution (30) incremental inconsistency parameter $d(\Delta\mu)$ can be obtained as

$$d(\Delta\mu) = \frac{{}^{old}\Phi - \mathcal{F}_{pq}\ (\mathcal{T}_{mnpq})^{-1}\ R_{mn}}{\mathcal{F}_{pq}\ (\mathcal{T}_{mnpq})^{-1}\ Z_{mn} - \Delta\mu\ \mathcal{F}_{pq}\ (\mathcal{T}_{mnpq})^{-1}\ \frac{\partial Z_{mn}}{\partial K_\alpha}\ H_{\alpha\beta}\ \frac{\partial\Phi^*}{\partial K_\beta} + \frac{\partial\Phi}{\partial K_\alpha}\ H_{\alpha\beta}\ \frac{\partial\Phi^*}{\partial K_\beta}} \tag{31}$$

where

$$\mathcal{F}_{pq} = \frac{\partial\Phi(\bar{T}_{ij}, K_\alpha)}{\partial\bar{T}_{pn}}\ \left(\bar{C}^e_{sq}\right)^{-1}\ \bar{T}_{sn} + \frac{1}{2}\ \frac{\partial\Phi(\bar{T}_{ij}, K_\alpha)}{\partial\bar{T}_{mn}}\ \bar{C}^e_{mk}\ \bar{\mathcal{L}}^e_{knpq} \tag{32}$$

Remark 4.2 In the limit, for small deformations, isotropic response, the increment inconsistency parameter $d(\Delta\mu)$ becomes

$$d(\Delta\mu) = \frac{{}^{old}\Phi - (n_{mn}\ E_{mnpq})\ \left(\delta_{im}\delta_{nj} + \Delta\mu\ \frac{\partial m_{mn}}{\partial\sigma_{pq}}\ E_{pqij}\right)^{-1}\ R^{old}_{mn}}{n_{mn}\ E_{mnpq}\ \left(\delta_{mp}\delta_{qn} + \Delta\mu\ \frac{\partial m_{pq}}{\partial\sigma_{ij}}\ E_{ijmn}\right)^{-1}\ {}^{n+1}m_{mn} + \frac{\partial\Phi}{\partial K_\alpha}\ H_{\alpha\beta}\ \frac{\partial\Phi^*}{\partial K_\beta}} \tag{33}$$

Upon noting that residual R_{pq} is defined in strain space, the increment inconsistency parameter $d(\Delta\mu)$ compares exactly with it's small strain counterpart [6]. This small deformation counterpart is used with the Hypo–elastic based integration algorithm.

5 Application to the Directional Shear Cell Apparatus

5.1 Computational Results

The DSC apparatus was extensively used in the late '80s at the University of Colorado at Boulder. For example [9] has used DSC apparatus in order to investigate shear behavior of various sands. In next we are presenting our numerical modeling of some of his experimental tests.

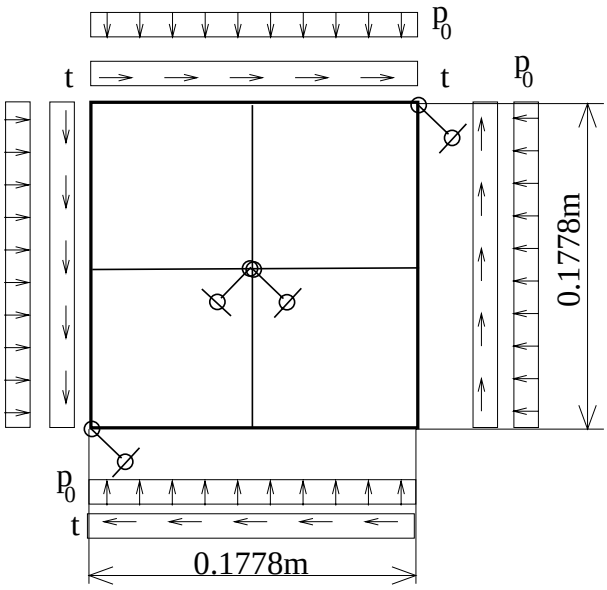

Figure 7: Numerical setup of a Directional Shear Cell test.

The finite element model used in numerical modeling of a DSC test is presented in Figure 7. It consists of four linear brick elements. Plain strain conditions are provided by restraining out of plane displacements. Loading is divided in two stages. The first stage comprises isotropic compression to target confinement state (in this case $p = 100.0$ kPa and $p = 180.0$ kPa). The second stage is a shear loading until instability occurs (instability in the experimental test, numerically we can follow the specimen beyond limit point). It is not clear if the instabilities (loss of control over loading process) were due to the bifurcation

phenomena inside the specimen or to the global rotation of the specimen. Since DSC is a load controlled device, only shear deformation of $\gamma_{xy} \simeq 3.5$ % was reached in the laboratory experiment.

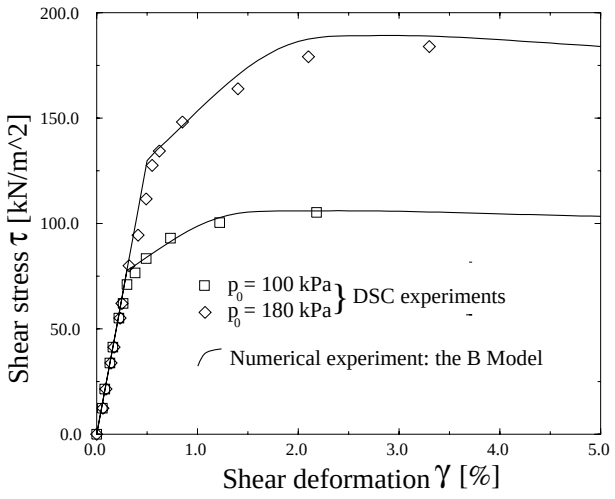

Figure 8: Numerical modeling of a test $K_0 14.5 - 30$. Shear stress – axial strain curves.

Figures 8 and 9 shows numerical modeling of a particular tests $K_0 14.5{-}30$ and $K_0 14.5{-}30$. Quite good agreement with the experimental test is obtained. In this Figure we show only numerical modeling up to 5% shear deformation to show the comparison between numerical and experimental tests.

The large shearing deformation extension of the previous test is presented in Figure 10. The post–peak region of the response curve is leveled for shear strains up to 30% but then starts to harden. Hardening is not a significant one and can be expected for such high shear deformation.

Figure 11 shows a deformation pattern at shear deformation of $\gamma = 150\%$. Considerable distortion can be observed. Large change of shape of the specimen can be used to explain the slight hardening in the post peak region of the response curve from Figure 10. Material inside the specimen moves quite a bit, thus crating an extra resistance to shearing. This

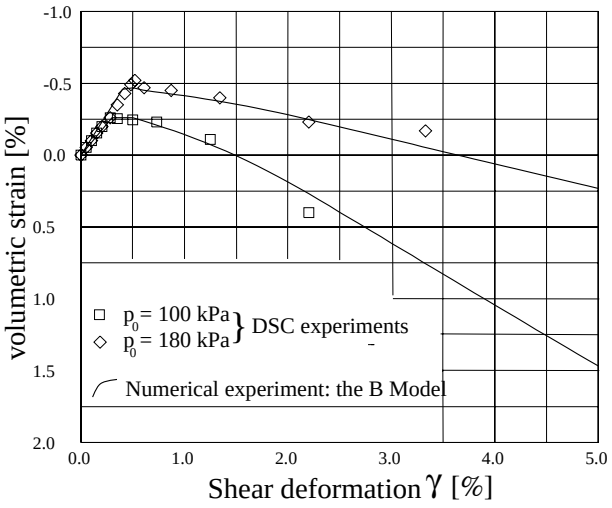

Figure 9: Numerical modeling of a test $K_0 14.5 - 30$ and $K_0 14.5 - 30$. Volumetric strain – axial strain curves

extra resistance is globally observed as slight hardening in the response curve.

6 Concluding Remarks

In this paper we have presented a new material model which is designed for large strain hyperelasto–plastic computations. The model features three analytical surfaces, representing yield limit, ultimate surface and plastic potential. Deviatoric trace of all three surfaces is pressure sensitive, having an almost triangular shape (Rankine yield criteria) for low confinement stresses and almost circular shape for high confinement stresses. Hardening and softening laws are of non–associate type, dependent on plastic work. Separation of hardening or softening for cone and cap portions of yield / potential surface is provided by means of switch function.

The numerical algorithm used for integrating hyperelasto–plastic constitutive relations utilizes Taylor's series expansion of elastic deformation tensor $\bar{C}^e_{ij}$. This approach removes

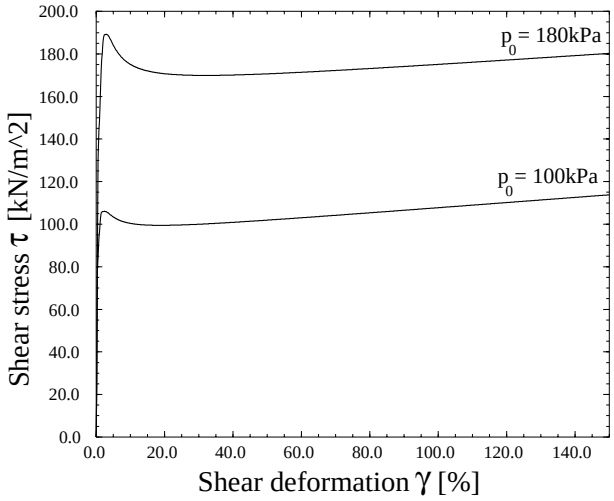

Figure 10: Large deformation extension of a test $K_0 14.5 - 30$.

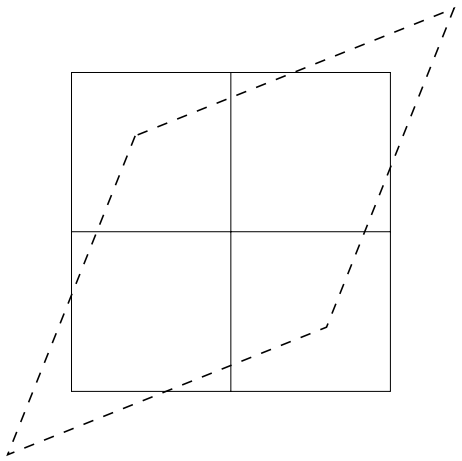

Figure 11: Typical deformation pattern for a large deformation numerical simulation of a shear test.

some of the restrictions posed by the spectral decomposition type of algorithms, widely used in literature.

A set of comparisons between DSC test results and numerical predictions were presented.

These comparisons show favorable characteristics of the material model and the integration algorithm for large deformation numerical simulations on geomaterials.

Acknowledgment

The authors gratefully acknowledge partial support by NASA Grant NAS8-38779 from Marshall Space Flight Center.

References

[1] N. C. Costes, V. C. Janoo, and S. Sture. Microgravity experiements on granular materials. In R. H. Doremus and P. C. Nordine, editors, *Material Research Society Symposium Proceedings*, volume 87, pages 203–212, 1987.

[2] E. A. de Souza Neto, D. Perić, M. Dutko, and D. R. J. Owen. Finite strain implementation of an elastoplastic model for crushable foam. In N.-E. Wiberg, editor, *Advances in Finite Element Technology*, pages 174–188, Barcelona, 1995. CIMNE.

[3] C. S. Desai, S. Somasundaram, and G. Frantziskonis. A hierarchical approach for constitutive modelling of geological materials. *International Journal for Numerical and Analytical Methods in Geomechanics*, 10:225–257, 1986.

[4] Bernard Halphen and Nguyen Quoc Son. Sur les matériaux standards généralisés. *Journal De Méchanique*, 14(1):39–63, 1975.

[5] R. Hill. *The Mathematical Theory of Plasticity*. The Oxford Engineering Science Series. Oxford at the Clarendon Press, 1st. edition, 1950.

[6] Boris Jeremić and Stein Sture. Implicit integrations in elasto–plastic geotechnics. *International Journal of Mechanics of Cohesive–Frictional Materials*, 2:165–183, 1997.

[7] Steen Krenk. Family of invariant stress surfaces. *ASCE Journal of Engineering Mechanics*, 122(3):201–208, 1996.

[8] Poul V. Lade. Double hardening constitutive model for soils, parameter determination and predictions for two sands. In A. Saada and G. Bianchini, editors, *Constitutive Equations for Granular Non–Cohesive Soils*, pages 367–382. A. A. Balkema, July 1988.

[9] Jerome J. McFadden. Experimental response of sand during pricipal stress rotations. Master of Science thesis, University od Colorado at Boulder, December 6 1988.

[10] J. C. Nagtegaal and J. E. de Jong. Some aspects of non–isotropic workhardening in finite strain plasticity. In E. H. Lee and R. L. Mallet, editors, *Plasticity of Metals at finite strains*, pages 65–106. Stanford University, 1981.

[11] S. Nemat–Nasser. On finite deformation elasto–plasticity. *International Journal of Solids and Structures*, 18(10):857–872, 1982.

[12] S. Nemat–Nasser. On finite plastic flow of crystalline solids and geomaterials. *Journal of Applied Mechanics*, 50:1114–1126, 1983.

[13] R. Nova and D. M. Wood. A constitutive model for sand in triaxial compression. *International Journal for Numerical and Analytical Methods in Geomechanics*, 3:255–278, 1979.

[14] M. Pastor, O. C. Zienkiewicz, and A. H. C. Chan. Generalized plasticity model for three–dimensional sand behaviour. In A. Saada and G. Bianchini, editors, *Constitutive Equations for Granular Non–Cohesive Soils*, pages 535–549. A. A. Balkema, July 1988.

[15] Carl E. Pearson, editor. *Handbook of Applied Mathematics.* Van Nostrand Reinhold Company, 1974.

[16] J. M. Pestana and A. J. Whittle. Compression model for cohesionless soils. *Géotechnique*, 45(4):611–631, 1995.

[17] J. C. Simo. Algorithms for static and dynamic multiplicative plasticity that preserve the classical return mapping schemes of the infinitesimal theory. *Computer Methods in Applied Mechanics and Engineering*, 99:61–112, 1992.

[18] S. Sture, K. Runesson, and E. J. Macari-Pasqualino. Analysis and calibration of a three invariant plasticity model for granular materials. *Ingenieur Archiv*, 59:253–266, 1989.

[19] Stein Sture. Hollow cylinder apparatuses, directional shear cells, and induced anisotropy in soils. Technical Report 59076-1, Norwegian Geotechnical Institute, May 1986.